DATA PAPER

Centrifuge Testing of Circular and Rectangular Embedded Structures with Base Excitations

Elnaz Esmaeilzadeh Seylabi,[a] M.EERI, Eva Agapaki,[b] Dimitris Pitilakis,[c] M.EERI, Scott Brandenberg,[b] M.EERI, Jonathan P. Stewart,[b] M.EERI, and Ertugrul Taciroglu,[b] M.EERI

We present data and metadata from a centrifuge testing program that was designed to investigate the seismic responses of buried circular and rectangular culverts. The specimen configurations were based on Caltrans Standard Plans, and the scope of research was to compare the experimental findings with the design method described in the *NCHRP Report 611* as well as to formulate preliminary recommendations for Caltrans practice. A relatively flexible pipe and a stiff box-shaped specimen embedded in dense sand were tested in the centrifuge at the Center for Geotechnical Modeling at University of California, Davis and were subjected to a set of broadband and harmonic input motions. Responses were recorded in the soil and in the embedded structures using a dense array of instruments. Measured quantities included specimen accelerations, bending strains, and hoop strains; soil accelerations, shear-wave velocities, settlements, and lateral displacements; and accelerations of the centrifuge's shaking table. This data paper describes the tests and summarizes the generated data, which are archived at DesignSafe.ci.org (DOI: 10.17603/DS2XW9R) and are accessible through an interactive Jupyter notebook. [DOI: 10.1193/110717EQS232DP]

INTRODUCTION

Seismic design of underground structures requires soil-structure–interaction (SSI) analyses, which are often decomposed into two subproblems. The "kinematic" SSI problem is concerned with the motion of the structure in the presence of spatially varying ground motions and the interface pressures that develop as a result of the stiffness contrast between the soil and the structure. The "inertial" SSI problem involves the determination of soil reactions that develop as a result of the inertial forces associated with the accelerations of the structure. The kinematic component of the SSI effect is generally considered to be more significant for buried structures, primarily because of the typically modest mass such structures have as well as their inherent confinement by the surrounding soils.

[a] Mechanical & Civil Engineering Department, California Institute of Technology, Pasadena, CA 91125
[b] Civil & Environmental Engineering Department, University of California, Los Angeles, CA 90095; Email: etacir@ucla.edu (E. T.)
[c] Department of Civil Engineering, Aristotle University of Thessaloniki, 54124 Thessaloniki, Greece

Earthquake Spectra, Volume 35, No. 3, pages 1485–1505, August 2019;

Classical and advanced limit equilibrium methods (e.g., Mononobe and Matsuo 1929, Xu et al. 2015) offer means to estimate the peak seismic earth pressures for many earth-retaining structures, but they usually are *not* the appropriate tools for seismic design of completely embedded structures, as they do not reflect the SSI processes that govern the evolution of the amplitude and distribution of interface pressures that develop during shaking. As such, specific procedures for buried structures were sought by the research community. For example, Wang (1993) proposed a pseudostatic deformation-based approach to take the effects of SSI into account in the seismic design of underground structures, followed by an update by Penzien (2000). These approaches were later summarized and applied to various design problems by Hashash et al. (2001). The aforementioned methods featured analytical (elasticity-based) formulas to compute the seismic bending moments and hoop forces of the embedded structures with circular cross-sections. Methods for computing the internal seismic forces for rectangular structures, on the other hand, were based on static frame analyses, the loading terms for which were produced by using the pseudostatic soil deformations. More recently, Katona (2010) presented a finite-elemen–based method to obtain the seismic responses of buried culverts and cut-and-cover tunnels, which is based on the application of linearly varying quasistatic displacement profiles at the lateral boundaries of a soil domain that contains the buried or embedded structure. The quasistatic displacements are specified as the product of free-field ground strains and the height of the modeled soil domain. It should be noted here that the pseudostatic method described in Wang (1993) is conceptually identical to that by Katona (2010), in that the former provides an analytical solution under simplifying assumptions (e.g., soil homogeneity), while the latter relaxes these assumptions and produces a numerical solution.

The inherent limitations of the quasistatic methods include the following: (1) the frequency content of the ground motion is only indirectly represented (i.e., in an average sense through their impact on the shear strain), which is known to be a first-order driver of seismic earth pressure for a given wave amplitude; (2) by conditioning the analyses on shear strain, the analyses are impacted by the challenges and limitations of one-dimensional ground response analyses (e.g., Stewart et al. 2014); (3) the shear strain field is assumed to be uniform over the height of the buried structure, which may not be a valid assumption depending on the frequency of the seismic excitation, the size of the underground structure, the heterogeneity of the soil profile, and the free-field wave propagation mode; and (4) neither the negative (because of lack of soil within the buried structure) or the positive (because of mass of the buried structure) inertia are considered.

Current seismic design practices, such as *NCHRP Report 611* (Anderson et al. 2008), are based on the procedure proposed by Wang (1993) for both circular and rectangular buried structures. Anderson et al. (2008) performed a series of parametric SSI analyses to verify that the NCHRP procedure can provide a reasonable estimate of deformations in culvert structures caused by transient ground deformations and concluded that the recommended procedure should be tested on a range of culvert configuration, ground condition, and earthquake shaking level to confirm that the NCHRP procedures are practical. Moreover, they identified that experimental studies are needed to confirm the validity of the recommended procedure.

In recent years, quite a number of experimental (e.g., Cilingir and Madabhushi 2011a, 2011b, Lanzano et al. 2012, 2013, Tsinidis et al. 2015, Ulgen et al. 2015, Abuhajar et al. 2015), numerical (e.g., Hashash et al. 2005, Kontoe et al. 2014, Lanzano et al. 2013, Tsinidis et al. 2016, Tsinidis 2017), and analytical (e.g., Bobet et al. 2008, Park et al. 2009, Bobet 2010) studies

Table 1. A list of previous experimental studies on response of buried structures in dry sand

	Structure		Input motion			
Authors	Type	Dimensions (m)	Type	PGA (g)	Frequency (Hz)	Soil relative density
Cilingir and Madabhushi (2011a, 2011b)		5 × 0.061				
	S	5 × 0.155	H	0.08–0.32	0.8–1.2	
	C	5 × 0.088	E	0.22–0.62	1–3	45%
Lanzano et al. (2012, 2013)	C	6 × 0.06	H	0.05–0.15	0.37–0.75	40%, 75%
Tsinidis et al. (2015)	S	5 × 0.13	H, SS	0.02–0.24	0.6–1.2	90%
Ulgen et al. (2015)	S	2 × 0.06	H	0.25–0.4	2–3.5	70%
Abuhajar et al. (2015)	S	4.57 × 0.27 4.57 × 0.53	E	0.11–0.33	0.46–1.45	50%, 90%

Note: All the quantities are provided in the prototype scale. In the third column, dimensions are in width thickness for square sections and in diameter thickness for circular sections. C, circle; H, hormonic; E, earthquake; S, square; SS, sine-sweep motions.

were conducted to explore the accuracy of the aforementioned simplified procedures. A nonexhaustive list of previously performed experimental studies, based on centrifuge modeling, on buried structures in dry sand is provided in Table 1. We have undertaken a centrifuge modeling program designed to extend the previous test results by (1) utilizing a wider range of ground motions with frequency content for which interaction effects are expected to range from significant to negligible, (2) applying a wider range of shaking amplitudes to investigate the effects of soil nonlinearity, and (3) deploying a relatively denser instrument configuration to enable measurement of detailed responses of the culvert section and the near- and far-field soils. We used the 9-m radius centrifuge at the Center for Geotechnical Modeling at University of California, Davis (Kutter et al. 1994) to perform the centrifuge experiment, consisting of two representative structures embedded in a granular soil selected per Caltrans Standard Plans "A62E" and "A62F" (Caltrans 2015).

The main objective of this research is to (1) develop a comprehensive set of experimental data on SSI behavior of buried culverts, (2) compare the experimental findings with the design method described in the NCHRP Report No. 611 (Anderson et al. 2008) and establish the validity (or lack thereof) of this method for the specific Caltrans configurations tested, and (3) formulate recommendations for Caltrans practice and identify future research needs in this area, as needed. In this manuscript, we provide only the details of the interactive data report prepared for this project and details of the centrifuge experiments that were performed. Results of investigations for the second and third objectives are deferred to subsequent publications.

INTERACTIVE DATA REPORT

Experimental data are often documented as a static report (e.g., as a pdf file) that presents relevant metadata, such as model sketches, sensor lists, event sequences, etc., and provides plots of the collected data. These reports provide guidance to users who wish to download the data and interact with it, but the reports themselves do not provide a level of interaction that users often require to learn from the data.

The data report for the project presented in this paper is an interactive report written in a Jupyter notebook that is housed in DesignSafe-CI (Rathje et al. 2017), which is the repository that also houses the data. A DesignSafe-CI registered user has access to the community version of the interactive data report. The readers can also download the data set along with the Jupyter notebook that includes an interactive data report (DOI: 10.17603/DS2XW9R, Esmaeilzadeh Seylabi et al. 2017). Jupyter notebooks combine code blocks, in which the data may be opened, processed, interrogated, and plotted, with markdown blocks that contain descriptions of the data. The text and figures in the report were written in HTML and coexist with Python code that directly interacts with the experimental data. Specific innovative features of the data report include:

1. An interactive data plotter in which users can select a specific event from a drop-down menu and subsequently plot data from any desired sensor (users are able to zoom in on desired portions of the data, extract specific data points of importance, e.g., the maximum value of a specific data quantity, and export any data plot as an image file).
2. An interactive model sketch is embedded as an "iFrame" object linked to an "Autodesk 360 drawing" object (users are able to zoom in and out to see various portions of the model configuration and can measure desired dimensions using the interactive tools).
3. Tables containing sensor lists, event sequences, etc., which are directly rendered from comma separated value files and presented in HTML format using the jQuery javascript (this eliminates the potential for a mismatch between the data report and the table maintained by the researchers).

The Jupyter notebook may be opened by any user with a DesignSafe account to explore our data set. Our notebook contains code for reading and plotting the data, and users can introduce their own code by downloading the notebook and customizing it for more detailed data analysis. The notebook may also be used as a template for users who wish to adapt it to their own data sets. These custom notebooks may then be published in DesignSafe for other users to access. Jupyter notebooks provide the opportunity to interact with the data on the DesignSafe servers so that users are not required to download the entire data set to work on it. This enables data sharing and curation to be a natural part of the project workflow.

CENTRIFUGE MODELING AND SCALING LAWS

In centrifuge modeling, we use scaling laws so that the stress field at any point within the model is similar to what is expected in the prototype. This allows us to capture the actual nonlinear and pressure-dependent behavior of the soil with the scaled model. Scaling laws (Madabhushi 2014) for different parameters relevant to our research are listed in Table 2, where N is the scaling factor.

CULVERT STRUCTURES

MECHANICAL PROPERTIES OF THE CULVERT STRUCTURES

The Caltrans Standard Plans (Caltrans 2015) present common configurations for culvert structures used in California. These culverts are composed of corrugated steel pipe or reinforced concrete box structures. The model structures, embedment depths, and soil properties utilized in the centrifuge tests were selected to be consistent with those commonly used culvert structures.

Table 2. Centrifuge modeling scaling laws used in this study

Parameter	Model/ prototype	Parameter	Model/ prototype	Parameter	Model/ prototype	Parameter	Model/ prototype
Length	$1/N$	Area	$1/N^2$	Mass	$1/N^3$	Stress	1
Strain	1	Force	$1/N^2$	Moment	$1/N^3$	Time (dynamic)	$1/N$
Frequency	N	Displacement	$1/N$	Velocity	1	Acceleration	N

Particularly, the selected pipe and box structures are expected to have a relatively flexible and stiff behavior with respect to the surrounding soil, which is a dense dry sand.

PIPE STRUCTURE

The full-scale prototype pipe structure is a 15.24 × 5.08 cm (6 × 2 in.) corrugated steel section with a thickness of 0.28 cm (0.111 in.) and an inside diameter of 2.44 m (8 ft.). The assumed mechanical properties for steel are the Young's modulus of $E = 200\,\text{GPa}$ ($2.9 \times 10^7\,\text{psi}$), the unit weight of $\gamma = 77.4\text{kN/m}^3$ ($0.285\,\text{lb/in.}^3$), and the Poisson's ratio of $\nu = 0.3$. Small-scale corrugated steel pipe appropriate for centrifuge modeling would be exceptionally difficult to fabricate and test. Therefore, we decided to replace the actual corrugated pipe with an equivalent uniform circular section made of aluminum. The controlling parameter is the section thickness. We selected the radius of the pipe large enough so that one can get access inside for strain gauging, which in turn resulted in choosing the scaling factor of $N \sim 20g$. Capturing both static and dynamic stiffnesses does not result in feasible practical section properties. We numerically explored the importance of satisfying each of these criteria and found that capturing the static stiffness would result in responses closer to the response of the prototype model, which is likely due to the response of the model being dominated by the soil rather than the first mode frequency of the culvert structure. Therefore, we decided to use the static flexural stiffness of the prototype corrugated steel pipe structure to obtain the thickness t_{model} of the equivalent section:

$$t_{\text{model}} = (12(EI)_{\text{prototype}}/E_{\text{model}})^{1/3} \tag{1}$$

where I is the cross-section moment inertia. This resulted in using a uniform seamless aluminum cylinder specimen with a thickness of 0.16 cm (0.065 in.) and inside diameter of 12.37 cm (4.87 in.). It is made of aluminum 6061-T6 with $E = 68.95\,\text{GPa}$ ($10^7\,\text{psi}$), $\gamma = 26.48\text{kN/m}^3$ ($0.0975\,\text{lb/in.}^3$), and $\nu = 0.33$ (all based on manufacturer specifications rather than measurements).

BOX STRUCTURE

The full-scale prototype reinforced-concrete structure is a 3.66 × 2.44 m (12 × 8 ft) rectangular section with roof, invert, and wall thicknesses of 26.7 cm (10.5 in.), 29.2 cm (11.5 in.), and 24.1 cm (9.5 in.), respectively. The model specimen is a box tube with inside dimensions of 18.4 × 10.8 cm (7.25 × 4.25 in.) and uniform thickness of 0.95 cm (0.375 in.). It is also made of aluminum 6061-T6. Because we are only interested in elastic-range behavior of the reinforced-concrete box, it is viable to choose metal as the material for the model. Moreover,

the mass density of aluminum and reinforced concrete are similar, and therefore, dynamic properties of boxes of either material with similar section properties are expected to be similar in the elastic range. Considering $N \sim 20g$, we determined the thickness of the specimen based on the flexural stiffness of the prototype box structure. The flexural stiffness of the prototype unit width cracked reinforced-concrete section can be computed as follows (Park and Paulay 1975):

$$(EI)_{\text{prototype}} = E_c a^3/3 + E_s A_s (d-a)^2 \tag{2}$$

where E_c and E_s are Young's modulus of concrete and steel, respectively; A_s is rebar area per unit width; d is the effective depth of the section; and a is the uncracked depth. For a normal weight and normal density concrete, E_c can be approximated as $57{,}000\sqrt{f'_c}$. The uncracked depth is:

$$a = \frac{A_s f_y}{0.85 f'_c} \tag{3}$$

where f'_c is compressive strength of concrete, and f_y is the yield strength of steel. According to the Caltrans Standard Plan D80, we consider #6 rebars with spacing of 11.43 cm (4.5 in.) and the rebar cover of 2.54 cm (1 in.). The average thickness of 26.7 cm (10.5 in.) is assumed. For $f'_c = 27.6$ MPa (4,000 psi), the concrete of Young's modulus is $E_c = 24.8$ GPa (3.6×106 psi). Assuming $f_y = 413.7$ GPa (60,000 psi), the average flexural stiffness of the box structure will be 48.3×10^{12} N.m (17.8×10^7 lb-in.). Using Equation 1 results in $t_{\text{model}} = 0.76$ cm. It should be noted that the main reason that the dimensions of the specimen are not the same as the targeted model is unavailability of prefabricated rectangular tube with the desired geometry.

STRAIN GAUGES

Strain gauges are used to measure the deformation of the culvert structures, which can also be used to evaluate dynamic increments of internal forces. As explained in the following section, our preliminary numerical simulations showed that both specimens would exhibit measurable strains during seismic loading. We measured bending and hoop strains using dense strain gauge arrays on the walls of each structure.

DETERMINATION OF IDEAL SENSOR POSITIONS

In order to determine the ideal positions for strain gauges, we modeled each structure numerically (with a setting similar to the centrifuge experiments). To this end, we used an in-house finite element code to solve the wave equations in the frequency domain. A two-dimensional plane strain model was constructed with eight-node quadrilateral elements. Periodic boundary conditions were applied along the left and right sides of the model to represent the effects of the container walls. Elastic homogeneous soil with shear-wave velocity of 198 m/s, unit weight of 17.5 kN/m^3, and Poisson's ratio of 0.3 were considered in all simulations. The properties of the box and pipe structures were set to values for aluminum. Using this model, the steady-state response of the structures were obtained over the range of frequencies from 0 to 25 Hz. More details can be found in Esmaeilzadeh Seylabi et al. (2017).

Figures 1 and 2 display the amplitudes of in-plane bending and hoop strain profiles for the pipe structure at 5, 14.5, and 25 Hz. These frequencies were specifically chosen because the computed strain energy within the structure was more significant at frequencies

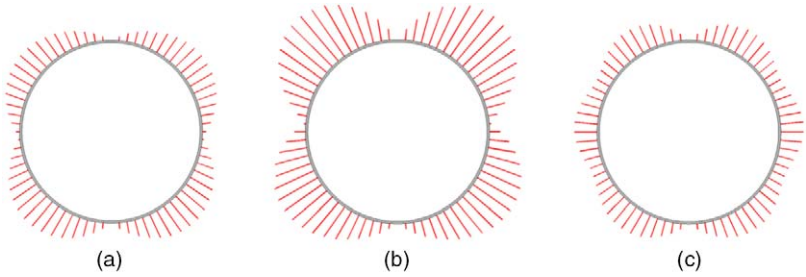

Figure 1. Amplitude of the steady-state bending strain profile of the pipe structure. (a) $f = 5$ Hz; (b) $f = 14.5$ Hz; (c) $f = 25$ Hz.

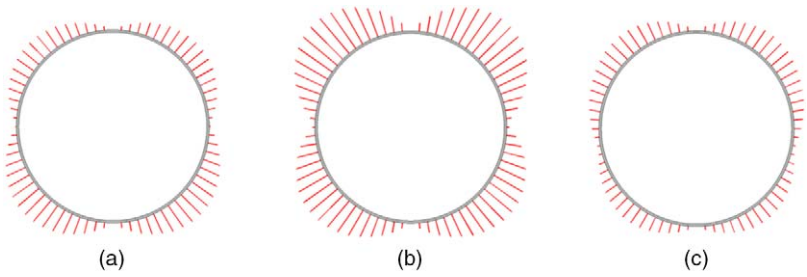

Figure 2. Steady-state hoop strain amplitude profile for the pipe structure. (a) $f = 5$ Hz; (b) $f = 14.5$ Hz; (c) $f = 25$ Hz.

close to the natural frequencies of the soil deposit, which are 4.95, 14.85, and 24.75 Hz (for $V_s = 198$ m/s and layer thickness of 10 m). The maximum bending strains occurred at $\theta = 45$, 135, 225, and 315 degrees.

Figure 3 displays the in-plane bending strain profiles for the box structure at the selected frequencies. The strain profiles along the walls and roof visually appear to conform with linear or second-order polynomial functions, whereas along the base, the strain profiles appear to be more compatible with third-order polynomials. In-plane axial (henceforth referred to as "hoop") strains are not shown for the box structure, as they had far smaller magnitudes than the bending strains.

Figure 4 shows the configuration of the strain gauges on the box and pipe structures.

We used OMEGA KFH-6-350-C1-11L3M3R strain gauges, which are prewired linear-pattern gauges with a nominal resistance of 350 Ω and three 3-m leads. The gauge dimensions are 10.5 × 3.9 mm, and the gauge factor is 2.04. The gauge factor is defined as follows:

$$GF = \frac{\Delta R/R}{\varepsilon} \tag{4}$$

where R is the resistance of the strain gauge, ΔR is the change in the electrical resistance, and ε is the measured strain. Using this gauge factor, the nominal sensitivity of the strain gauges

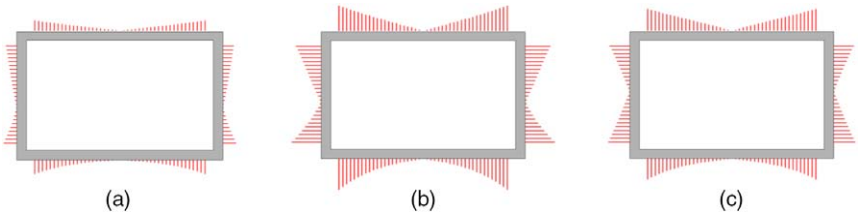

Figure 3. Steady-state hoop strain amplitude profile for the box structure. (a) $f = 5$ Hz; (b) $f = 14.5$ Hz; (c) $f = 25$ Hz.

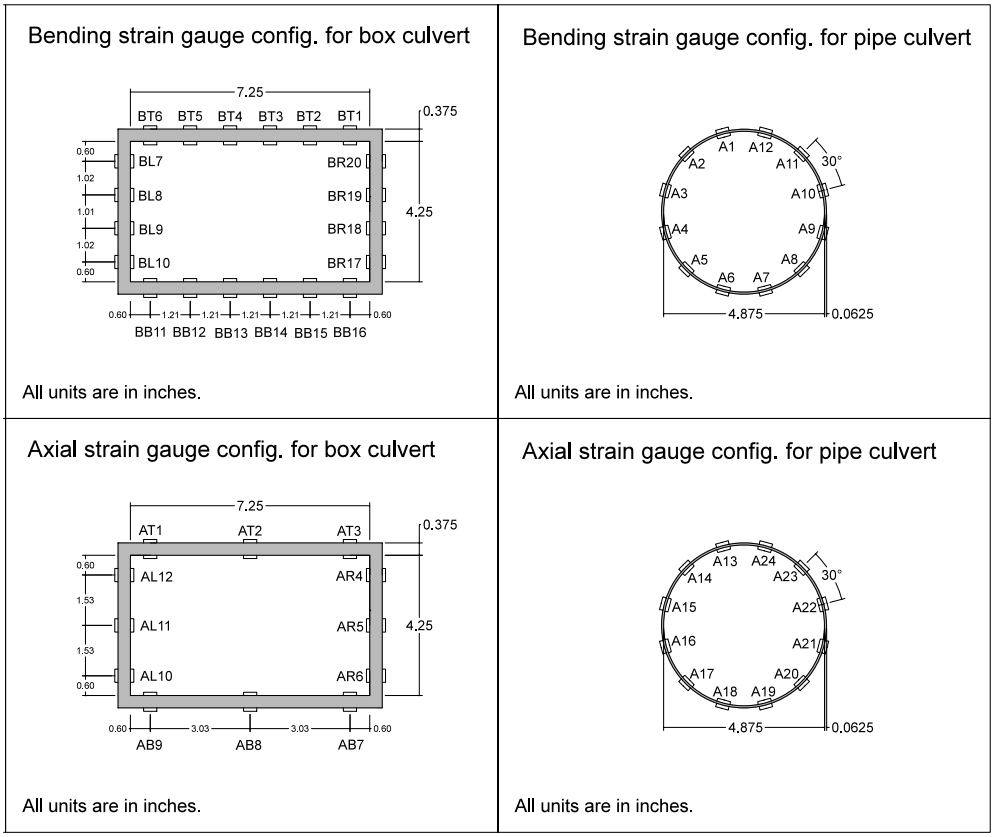

Figure 4. Strain gauge configurations.

can be obtained. We used a Wheatstone full bridge to measure both bending and hoop strains. Therefore, for the bending strain ε_b:

$$\frac{\Delta V}{V} = GF\varepsilon_b \tag{5}$$

and for the hoop strain ε_h:

$$\frac{\Delta V}{V} = GF\frac{1+\nu}{2}\varepsilon_h\,. \tag{6}$$

For a Wheatstone full-bridge configured to measure the bending strain, the nominal sensitivity is 2.04, and for the hoop full strains, it is 1.36. The latter is obtained by multiplying the gauge factor by $(1+\nu)/2$, wherein $\nu = 0.33$ is the Poisson's ratio for aluminum.

For the gauge bonding inside and outside of the box, we used an Omega TT300 complete heat cure adhesive kit following a specific curing procedure of applying a uniform pressure of about 207 kPa (30 psi) for 2 h at the temperature of 125°C. In order to accelerate the process, we used the clamp mechanism shown in Figure 5 for installing multiple gauges simultaneously. Affixing the strain gauges to the inside of the pipe was difficult because of the curved surface and the small diameter of the pipe. Applying the specified pressure for the required duration ruled out the use of the TT300 adhesive. As an alternative, we used the instant Omega SG496 adhesive to install the gauges manually, one pair at a time. This adhesive is not as durable as the TT300, which results in a shorter service life. However, the solution was acceptable for a single test. Figure 6 displays the steps we took for the installation. A camera was placed inside the pipe to aid the alignment and placement of the strain gauges.

SOIL PROPERTIES

MECHANICAL PROPERTIES OF THE OTTAWA SAND

We used Ottawa sand in the experiments, which is a pure quartz sand composed of naturally rounded grains. Representative mechanical properties of the Ottawa sand are shown in Table 3.

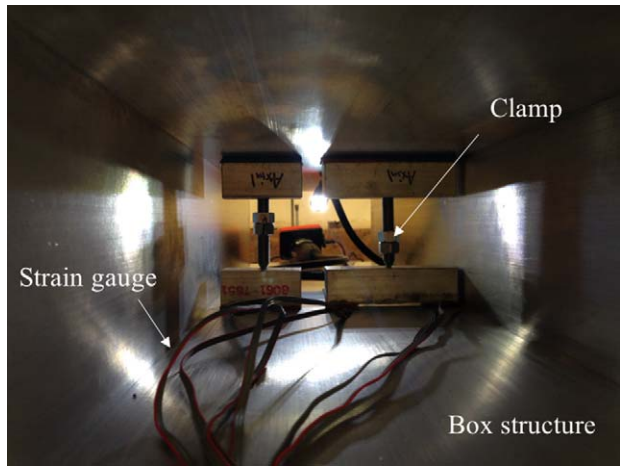

Figure 5. The clamp used for installing the strain gauges inside the box.

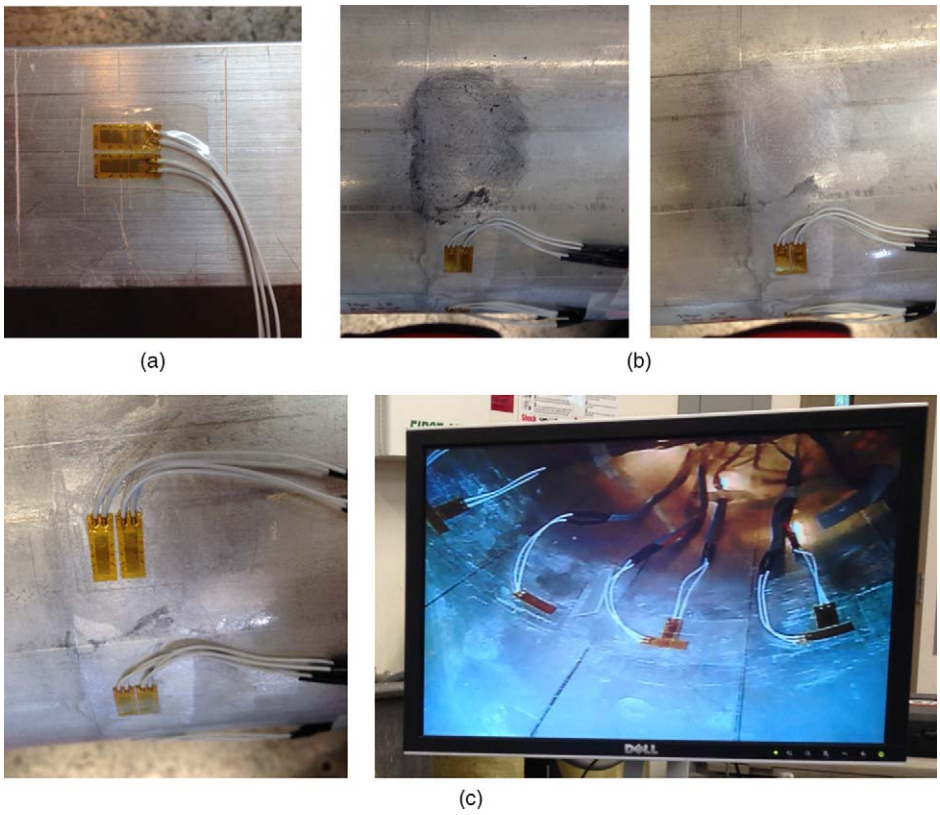

Figure 6. Installation of strain gauges inside and outside of the pipe. (a) Gauge alignment on auxillary bar; (b) surface cleaning; (c) gauge installation outside and inside the pipe.

AIR PLUVIATION TRIALS

We sought to place the sand in a dense state to represent the compacted select granular fills utilized in Caltrans culvert construction practice (in consulation with Caltrans engineers). An additional benefit of testing dense sand is that loose sands tend to densify during shaking, thereby resulting in an evolution of relative density during the testing sequence, whereas dense sand tends not to experience significant changes of state when vibrated. This simplifies interpretation of the test results. Therefore, we pluviated the sand at an average relative

Table 3. Mechanical properties of the Ottawa sand (Center for Geotechnical Modeling, *pers. comm.*, 2015)

Soil parameter	Value	Soil parameter	Value
Specific gravity, G_s	2.673	Mean grain size, D_{50}	≈0.2 mm
Coefficient of uniformity, C_u	1.73	Coefficient of gradation, C_c	1.08

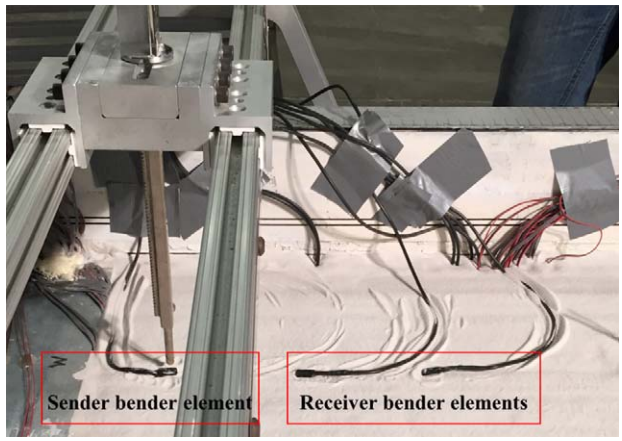

Figure 7. One array of the bender elements used for measuring shear-wave velocity.

density of 93%. Details of the trial tests conducted to achieve this relative density are provided in Esmaeilzadeh Seylabi et al. (2017).

SHEAR-WAVE VELOCITY

We used arrays of bender elements (e.g., Brandenberg et al. 2006) embedded at different locations in the model to measure shear-wave velocity (see Figure 7). Each array consists of three bender elements positioned 10 cm apart, one source and two receivers. The measurements are taken during the spinning at the centrifugal acceleration of $20g$. A high-voltage step wave motion is imposed on the source bender element, which causes the element to rapidly bend, inducing a horizontally propagating shear wave with vertical particle motion. The wave travels through the soil and deforms the receivers, resulting in a recorded voltage signal. The sign of the excitation is then reversed, causing the bender element to be excited in the opposite direction. Shear waves reflect the opposite polarization of these two source functions, while the *P*-waves emanating from the tip of the bender element do not. Therefore, averaging the positive and the negative of the reversed signal suppresses the *P*-wave arrival and enhances the shear-wave arrival, thereby enabling a more accurate travel time pick. Shear-wave velocity is then estimated by measuring the time it takes for the waves to travel between the receivers. The recorded signals were baseline corrected and filtered prior to using frequency-domain cross-correlation of the receiver signals to identify the travel time, as explained by Agapaki et al. (2016).

Shear-wave velocity is known to be a function of mean effective stress (σ'_m; e.g., Hardin and Drnevich 1970) for granular soils. Agapaki et al. (2016) regressed the data using three different functions, two of which were power laws that result in $V_s = 0$ at $\sigma_m = 0$ (Hardin and Drnevich 1970, Roesler 1979), and the third was a form that permits $V_s > 0$ at $\sigma'_m = 0$. The regression results are displayed in Figure 8. The form that best fits the data is given by Equation 7:

$$V_s(\mathrm{m/s}) = 141.6 + 92.1\left(\frac{\sigma'_m}{p_a}\right)^{0.35}. \tag{7}$$

where p_a is the atmospheric pressure.

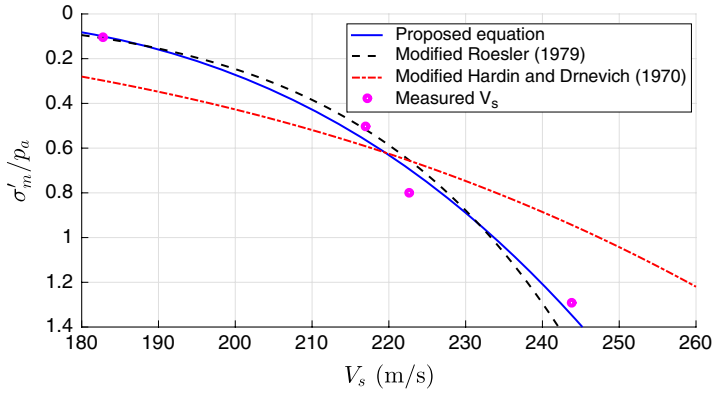

Figure 8. Relationship between V_s and σ'_m.

MODEL CONFIGURATION

MODEL CONTAINER

We used the NEES@UCDavis Flexible Shear Beam Container 2. The length, width, and height of this container are shown in Figure 9.

SENSORS

We used four types of sensors to measure the response of the model during shaking. Sensors utilized during the test included linear pattern prewired strain gauges to

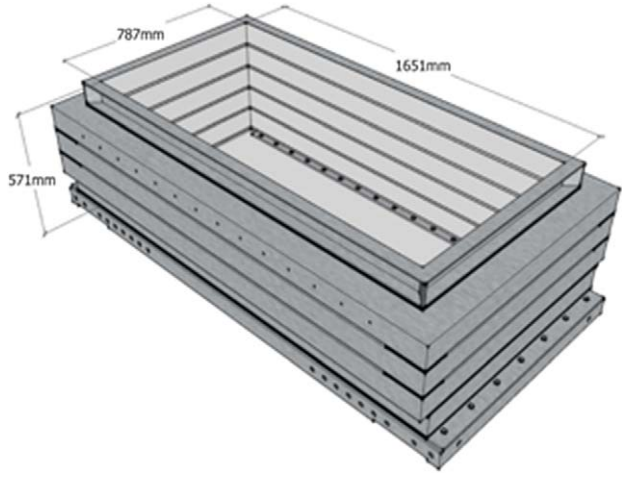

Figure 9. A schematic drawing of the flexible shear beam container used in this study (D. Wilson, *pers. comm.*, 2017).

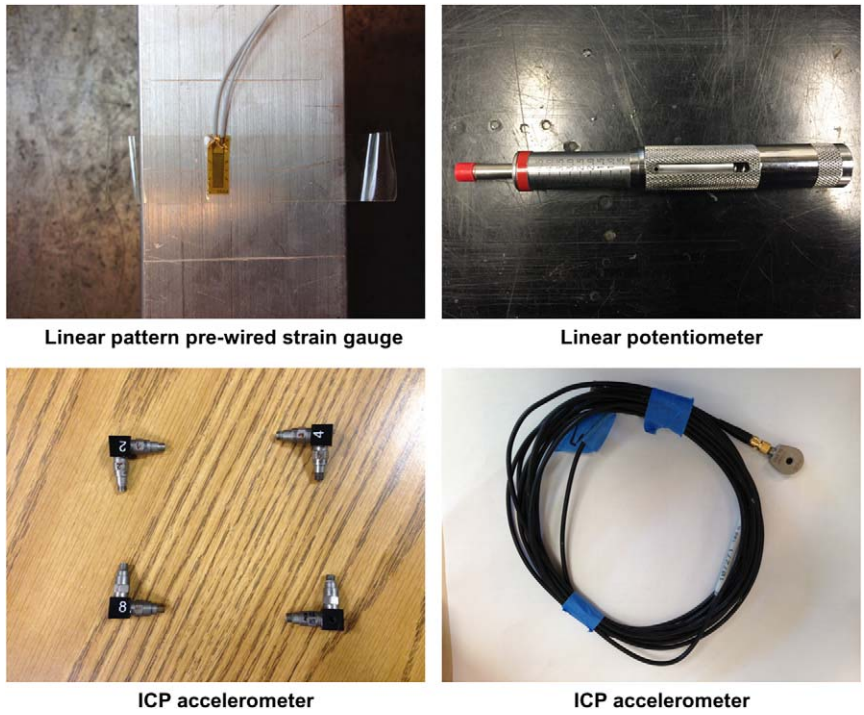

Figure 10. Sensor types used in the centrifuge tests.

measure both bending and hoop strains, bender elements to measure the shear-wave velocity, linear potentiometers (LPs) by BEI Sensors to measure soil settlements and lateral displacements, and ICP accelerometers by PCB Piezotronics to measure horizontal and vertical accelerations at various locations on the container, specimens, and in the soil. Figure 10 displays these sensors. Bender elements are shown in Figure 7.

MODEL CONSTRUCTION

Using the same procedure that was employed in air pluviation trials (see above), we pluviated the Ottawa sand into the model container in 2.5-cm–thick layers. We vacuumed the surface of each layer to make it level. We placed the pipe and box structures such that the soil cover for the specimens were 15.24 cm (0.5 ft) and 3 cm (0.1 ft), respectively. These soil covers are in accord with Caltrans Standard Plans. In order to make the soil compact around the specimens, we used a hand-held vibrator. Finally, we placed a thin 0.5-cm layer of Monterey sand above the last layer to prevent wind erosion during the spinning. Figure 11 displays the elevation view of the centrifuge model. Sensors were placed in six stages at different elevations in the model, including 59 accelerometers, 43 of which were installed in the soil or on the container, while the rest were on the specimens. We mounted a frame on top of the container to secure LPs in order to

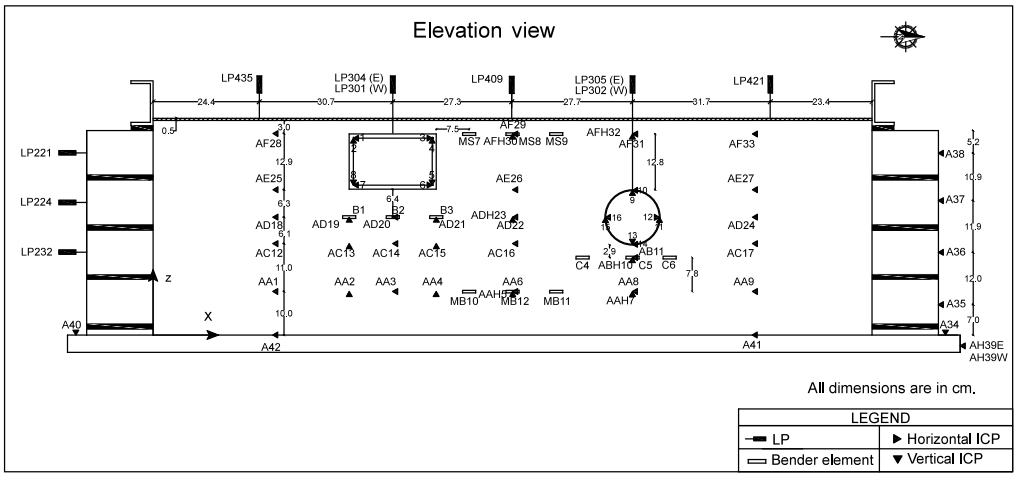

Figure 11. Elevation view of the centrifuge model.

measure soil surface settlements and to capture the vertical displacements of the specimens. We used another frame to attach LPs to the container wall and to measure the associated lateral displacements. We connected all sensors in the model to a data acquisition system. We used thin aluminum sheets to close the two ends of each specimen in order to avoid intrusion of sand inside the specimens. The plan views of the centrifuge model at different elevations and the configurations and labels of all the sensors are provided in Esmaeilzadeh Seylabi et al. (2017). The identifiers used for labeling the sensors, along with their positions, are provided in table 3 of the interactive data report (Esmaeilzadeh Seylabi et al. 2017).

GROUND MOTIONS

We applied a total of 25 shaking events to this model at $N \sim 20g$ centrifugal acceleration. Shaking was applied transverse to the culverts' long axes in the north-south direction (Figure 11). The sequence of the type of motions used to shake the model, including step, earthquake, and sinusoidal functions, are provided in Table 4. Three earthquake ground motions are used in this study, which are obtained from the PEER Ground Motion Database. The characteristics of these motions (i.e., target earthquake motions) are provided in Table 5. Figure 12 shows the 5%-damped spectral accelerations and the Arias intensity time series of the target earthquake motions.

It should be noted here that the shake table on the centrifuge cannot perfectly reproduce a target motion, and as a result, we applied some signal modifications. First, we increased the high-frequency content relative to the target motion when we computed the command motion. This accounts for a loss of high-frequency content because of the mechanics of the shake-table feedback control system. Then, we compared the achieved motion to the target motion and adjusted the command motion. Through an iterative process, the achieved base motions are similar to, but not equivalent with, the target motions. For this reason,

Table 4. The sequence of the input motions used in the centrifuge tests

Command input type	Applied amplification factor	Duration (s)	Command input file name	Measured data file name
Step function	0.6	–	01-Step.txt	01_01142016142113142814 46.5rpm
Step function	1.5	–	02-Step.txt	02_01142016142113144623 46.6rpm
Earthquake MUL279	0.1	8.92	03-RSN953_NORTHR_MUL279.shk	03_01142016142113151132 46.3rpm
Earthquake SMT090	0.1	12.18	04-RSN1077_NORTHR_STM090.shk	04_01142016142113153205 46.3rpm
Earthquake HEC000	0.33	6.31	05-HEC000.shk	05_01142016142113154433 46.2rpm
Earthquake MUL279	0.5	7.80	03-RSN953_NORTHR_MUL279.shk	06_01142016142113155045 46.2rpm
Earthquake SMT090	0.5	6.43	04-RSN1077_NORTHR_STM090.shk	07_01142016142113155556 46.3rpm
Earthquake HEC000	1	4.74	05-HEC000.shk	08_01142016142113155925 46.3rpm
Earthquake MUL279	1	7.69	03-RSN953_NORTHR_MUL279.shk	09_01142016142113160353 46.3rpm
Earthquake SMT090	1	5.20	04-RSN1077_NORTHR_STM090.shk	10_01142016142113162859 46.5rpm
Earthquake HEC000	3	4.68	05-HEC000.shk	11_01142016142113163253 46.5rpm
Sine sweep 1 (constant acceleration)	1	–	12-input_command.txt	12_01142016142113164528 46.4rpm
Sine sweep 1 (constant acceleration)	3	–	13-input_command.txt	13_01142016142113164949 46.4rpm
Sine sweep 2 (constant acceleration)	1	–	14-sw-25to500-0.3g-iter00	14_01152016094202113752 46.6rpm
Sine sweep 3	0.5	–	15-sw-25to500-0.1g-iter01	15_01152016094202120018 46.5rpm
Sine sweep 3	0.1	–	16-sw-25to500-0.1g-iter01	16_01152016094202121842 46.2rpm
Stepped sine 1 (iteration 0)	1	–	17-sine-0.1g-iter00	17_01152016094202125312 46.4rpm
Stepped sine 2 (iteration 1)	1	–	18-sine-0.1g-iter01	18_01152016094202134531 46.3rpm
Stepped sine 3 (iteration 2)	1	–	19-sine-0.1g-iter02	19_01152016094202135809 46.3rpm
Stepped sine 4 (iteration 3)	1	–	20-sine-0.1g-iter03	20_01152016094202143701 46.4rpm
Stepped sine 5 (iteration 4)	3	–	21-sine-0.1g-iter04	21_01152016094202145451 46.4rpm
Stepped sine 6 (iteration 5)	3	–	22-sine-0.1g-iter05	22_01152016094202151455 46.4rpm
Stepped sine 7 (iteration 6)	5	–	23-sine-0.1g-iter06	23_01152016094202152319 46.5rpm
Sine sweep 4 (constant velocity)	0.5	–	24-ExponentialSineSweep.shk	24_01152016094202153143 46.3rpm
Sine sweep 4 (constant velocity)	0.75	–	25-ExponentialSineSweep.shk	25_01152016094202154118 46.3rpm

Table 5. Characteristics of the earthquake ground motions used in this study

Earthquake	Year	Station	Component	Magnitude	R_{jb} (km)	V_{s30} (m/s)
Northridge	1994	Beverly Hills	MUL279	6.69	9.44	355.81
Northridge	1994	Santa Monica City Hall	STM090	6.69	17.28	336.20
Hector Mine	1999	Hector	HEC000	7.13	10.35	726.00

measured base motions should be used when interpreting the test data. The 5%–95% duration of the measured base motions for earthquake events are shown in Table 4.

We used the sine-sweep motions primarily to shake the model to prototype frequencies up to 25 Hz. As mentioned before, it was expected that soil-structure interaction effects would be more significant at higher frequencies. We used two types of constant acceleration and constant velocity target motions and found that the constant-velocity motions could provide command inputs with richer high-frequency energy content. We also used the stepped-sine signals to shake the model at discrete frequencies of 1.25, 1.85, 2.5, 3.75, 5, 7.5, 10, 17.5, and 25 Hz. For each iteration, we updated the amplitudes of the stepped-sine functions at different frequencies so that the amplitude of measured accelerations at the soil surface (as recorded by sensor AFH30) were nearly the same at all of the discrete frequencies considered. Figure 13 shows sample acceleration time series recorded at the first (iteration 0) and last (iteration 6) iterations. The dashed lines in Figure 13b show how successfully we updated the command motion to achieve almost constant amplitude acceleration time series at the soil surface. It should be noted that, ideally, a sine-sweep function could be used for this purpose. However, calibration of the command input using sine-sweep functions was not straightforward. This is why stepped sine functions were applied. Shaking the models with motions with the same

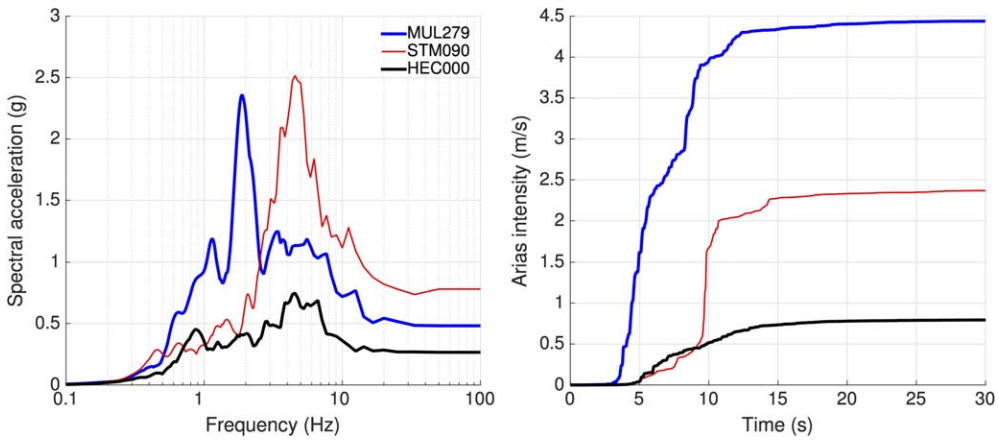

Figure 12. 5%-damped spectral acceleration and Arias intensity time series of the earthquake motions used in this study.

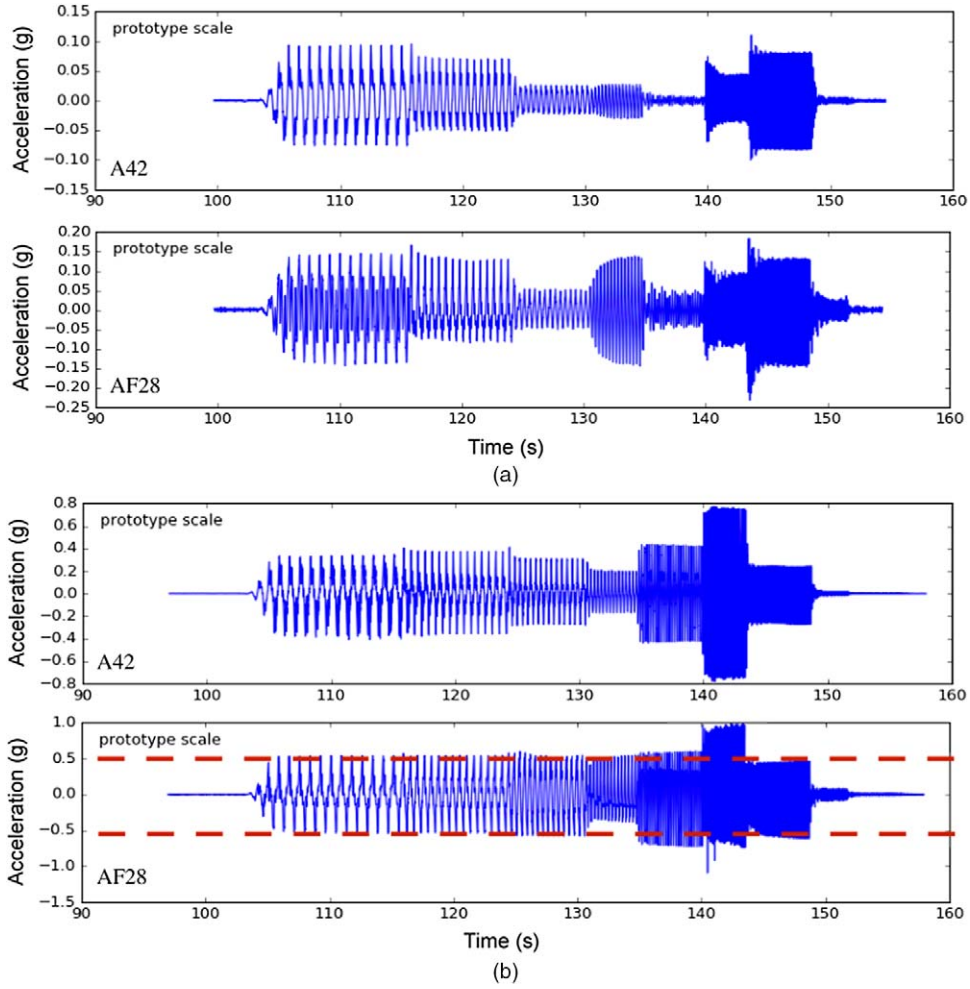

Figure 13. Acceleration time series recorded at A42 and AF28 for (a) shake event "Stepped sine 1 (iteration 0)" and (b) shake event "Stepped sine 7 (iteration 6)."

surface acceleration amplitude permits direct observations of the frequency dependence of the structural response.

SAMPLE DATA

In order to demonstrate the quality of the recorded data as well as the format of the figures that can be downloaded from the interactive data report (Esmaeilzadeh Seylabi et al. 2017), we present the time series of a number of sensors in this section. Figure 14 shows acceleration time series for sensors A42, AD18, AF28, and AF29 in prototype scale (Figure 11). Figure 15 shows the strain time series for the box and pipe structures for both in-plane bending and hoop strains. BL10 and AL10 are, respectively, the

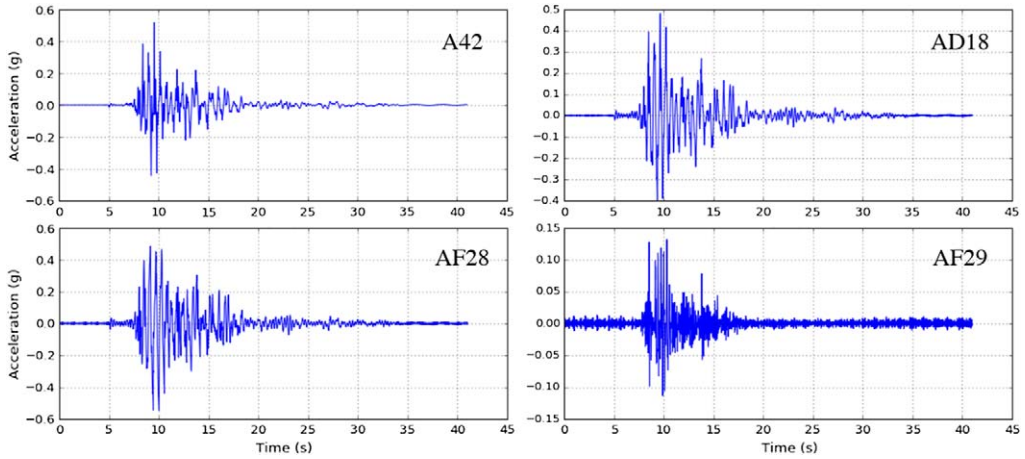

Figure 14. Sample acceleration time series recorded for shake event "Earthquake MUL279."

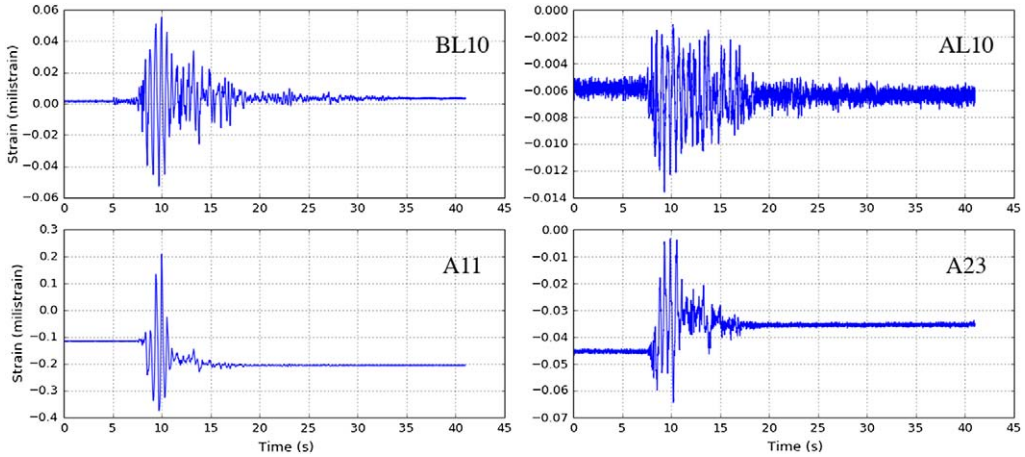

Figure 15. Sample in-plane bending and hoop strain time series recorded for shake event "Earthquake MUL279" on the box and pipe structures.

bending and hoop strains recorded at the bottom edge of the left wall of the box. A11 and A23 are, respectively, the bending and hoop strains recorded on the pipe at $\theta = 45$ degrees (see Figure 4). Both bending and hoop strain time series suffer from a static offset that is significant in the tested pipe structure, which is relatively flexible. Although the interpretation of the results is beyond the focus of this data paper, we think the observed offsets are mainly due to the changes in the soil confining pressure during the shake events. We will investigate this effect in more detail later.

KNOWN LIMITATIONS OF MEASURED DATA AND MODEL

All of the sensor time series plotted in the interactive data report are truncated to only include the part of signal that includes the main shake but are otherwise unprocessed. Application of appropriate filtering and signal processing methods are required to obtain the velocities, transient displacements, and other features of the dynamic response. After excavation, we noticed that one of the wires of the BT3 bridge was slightly damaged, which may affect the recorded data. Moreover, BL8 and AR5 bridges were not wired correctly. We also noticed that six of the ICPs inside the pipe specimen, which are labeled 11, 12, 13, 14, 15, and 16, were detached from the structure. However, by checking the signals visually, it seems that these detachments had happened after the shaking runs. It should be noted that we have not excluded data from any sensors that did not function properly in the interactive data plotter available at DesignSafe.ci.

ACKNOWLEDGMENTS

The authors would like to express their thanks to all staff members of the Center for Geotechnical Modeling at University of California, Davis for providing support during the experiment as well as Caltrans Engineers Carl Duan and Peter Lee for their guidance and assistance. The work presented here was funded by the California Department of Transportation (Caltrans), United States (Grant Number 65A0561). Any opinions, findings, and conclusions or recommendations expressed in this paper are those of the authors and do not necessarily reflect the views of the Caltrans.

REFERENCES

Abuhajar, O., Naggar, H. E., and Newson, T., 2015. Experimental and numerical investigations of the effect of buried box culverts on earthquake excitation, *Soil Dynamics and Earthquake Engineering* **79**, 130–148.

Agapaki, E., Esmaeilzadeh Seylabi, E., Brandenberg, S. J., Stewart, J. P., and Taciroglu, E., 2016. Centrifuge modeling of culvert structures to evaluate seismic earth pressures arising from soil-structure interaction, in *1st International Conference on Natural Hazards & Unfrastructure*, 28–30 June, 2016, Chania, Greece.

Anderson, D. G., Martin, G. R., Lam, I., and Wang, J. N., 2008. *NCHRP Report 611: Seismic Analysis and Design of Retaining Walls, Buried Structures, Slopes, and Embankments*, Transportation Research Board, Washington, DC.

Bobet, A., 2010. Drained and undrained response of deep tunnels subjected to far-field shear loading, *Tunneling and Underground Space Technology* **25**, 21–31.

Bobet, A., Fernande, G., Huo, H., and Ramirez, J., 2008. A practical iterative procedure to estimate seismic-induced deformations of shallow rectangular structures, *Canadian Geotechnical Journal* **45**, 923–938.

Brandenberg, S. J., Choi, S., Kutter, B. L., Wilson, D. W., and Santamarina, J. C., 2006. A bender element system for measuring shear wave velocities in centrifuge models, in *6th International Conference on Physical Modeling in Geotechnics*, Taylor & Francis, London, UK, 165–170.

Caltrans, 2015. Standard Plans (2015 edition), http://www.dot.ca.gov/hq/esc/oe/project_plans/HTM/stdplns-US-customary-units-new15.htm.

Cilingir, U., and Madabhushi, S. P. G., 2011a. Effect of depth on the seismic response of square tunnels, *Soils and Foundations* **51**, 449–457.

Cilingir, U., and Madabhushi, S. P. G., 2011b. A model study on the effects of input motion on the seismic behavior of tunnels, *Soil Dynamics and Earthquake Engineering* **31**, 452–462.

Esmaeilzadeh Seylabi, E., Agapaki, E., Pitilakis, D., Brandenberg, S. J., Stewart, J. P., and Taciroglu, E., 2017. Development of validated methods for soil-structure interaction analysis of buried structures, doi:10.17603/DS2XW9R.

Hardin, B. O., and Drnevich, V. P., 1970. *Shear Modulus and Damping in Soils, Tech. Rep*. Universtiy of Kentucky, Lexington, KY.

Hashash, Y. M. A., Hook, J. J., Schmidt, B., and Yao, J. I., 2001. Seismic design and analysis of underground structures, *Tunneling and Underground Space Technology* **16**, 247–293.

Hashash, Y. M. A., Park, D., and Yao, J. I. -C., 2005. Ovaling deformations of circular tunnels under seismic loading, an update on seismic design and analysis of underground strucrures, *Tunneling and Underground Space Technology* **20**, 435–441.

Katona, M. G., 2010. Seismic design and analysis of buried structures with CANDE-2007, *Journal of Pipeline Systems Engineering and Practice* **1**, 111–119.

Kontoe, S., Avgerinos, V., and Potts, D. M., 2014. Numerical validation of analytical solutions and their use for equivalent linear seismic analysis of circular tunnels, *Soil Dynamics and Earthquake Engineering* **66**, 206–219.

Kutter, B. L., Idriss, I. M., Kohnke, T., Lakeland, J., Li, X. S., Sluis, W., Zeng, X., Tasuscher, R. C., Goto, Y., and Kubodera, I., 1994. Design of a large earthquake simulator at UC Davis, *In Centrifuge* **94**, 169–175.

Lanzano, G., Billota, E., Russo, G., and Siverstri, F., 2013. Experimental and numerical study on circular tunnels under seismic loading, *European Journal of Environmental and Civil Engineering* **19**, 539–563.

Lanzano, G., Billota, E., Russo, G., Silvestri, G., and Madabhushi, S. P. G., 2012. Centrifuge modeling of seismic loading on tunnels in sand, *Geotechnical Testing Journal* **35**, 854–869.

Madabhushi, G., 2014. *Centrifuge Modeling for Civil Engineers*, CRC Press, Boca Raton, FL.

Mononobe, N., and Matsuo, M., 1929. On the determination of earth pressures during earthquakes, *Word Engineering Congress* **9**, 179–187.

Park, K. H., Tantayopin, K., Tantavanich, B., and Owastsiriwong, A., 2009. Analytical solution for seismic-induced ovaling of circular tunnel lining under no-slip interface conditions: a revisit, *Tunneling and Underground Space Technology* **24**, 231–235.

Park, R., and Paulay, T., 1975. *Reinforced Concrete Structures*, John Wiley & Sons, Hoboken, NJ.

Penzien, J., 2000. Seismically induced racking of tunnel linings, *International Journal of Earthquake Engineering and Structural Dynamics* **29**, 683–691.

Rathje, E. M., Dawson, C., Padgett, J. E., Pinelli, J. -P., Stanzione, D., Adair, A., Arduino, P., Brandenberg, S. J., Cockerill, T., Dey, C., Esteva, M., Haan, Jr., F. L., Hanlon, M., Kareem, A., Lowes, L., Mock, S., and Mosqueda, G., 2017. DesignSafe: New cyberinfrastructure for natural hazards engineering, *Natural Hazards Review* **18**.

Roesler, S. K., 1979. Anisotropic shear modulus due to stress anisotropy, *Journal of Geotechnical Engineering* **105**, 871–888.

Stewart, J. P., Afshari, K., and Hashash, Y. M. A., 2014. *Guidelines for Performing Hazard-Consistent One-Dimensional Ground Response Analysis for Ground Motion Prediction, PEER Report No. 2014/16*, Pacific Earthquake Engineering Research Center, Berkeley, CA.

Tsinidis, G., 2017. Response characteristics of rectangular tunnels in soft soil subjected to transversal ground shaking, *Tunneling and Underground Space Technology* **62**, 1–22.

Tsinidis, G., Pitilakis, K., Madabhushi, G., and Heron, C., 2015. Dynamic response of flexible square tunnels: Centrifuge testing and validation of existing design methodologies, *Géotechnique* **65**, 401–417.

Tsinidis, G., Pitilakis, K., and Madabhushi, G., 2016. On the dynamic response of square tunnels in sand, *Engineering Structures* **125**, 419–437.

Ulgen, D., Saglam, S., and Ozkan, M. Y., 2015. Dynamic response of a flexible rectangular underground structure in sand: Centrifuge modeling, *Bulletin of Earthquake Engineering* **13**, 2547–2566.

Wang, J., 1993. *Seismic Design of Tunnels: A Simple State-of-the-Art Design Approach*, Parsons Brinckerhoff, New York, NY.

Xu, X. -Y., Shamsabadi, A., and Taciroglu, E., 2015. Evaluation of active and passive seismic earth pressures considering internal friction and cohesion, *Soil Dynamics and Earthquake Engineering* **70**, 30–47.

(Received 2 November 2017; Accepted 22 February 2019)